MATHEMATICAL MODELING AND COMPUTING, Vol. 12, No. 4, pp. 1367–1380 (2025)

Computer Modeling of Memristive Electromagnetic Radiation Effect on a Five-Dimensional Neural Network

Kopp M. I.

Institute for Single Crystals, NAS Ukraine, Nauky Ave. 60, Kharkiv 61072, Ukraine

(Received 21 April 2025; Revised 13 October 2025; Accepted 20 October 2025)

This paper introduces a novel five-dimensional memristive artificial neural network (ANN) incorporating a flux-controlled memristor to model the effects of external electromagnetic radiation on neuronal dynamics. The network is mathematically formulated as a six-dimensional nonlinear dynamical system, where the additional dimension accounts for the memristive state variable. A comprehensive dynamical analysis is performed, including bifurcation diagrams, Lyapunov exponents, Kaplan-Yorke dimension, time-domain responses, and phase portraits, revealing complex chaotic behaviors. The theoretical predictions are validated through electronic circuit simulations using Multisim software. Furthermore, a synchronization model incorporating two coupled memristive subnetworks is developed to emulate interregional synchronization phenomena observed in biological neural systems.

Keywords: *artificial neural networks (ANNs); memristor; chaotic behavior; circuit implementation; synchronization.*

2010 MSC: 34A34, 37D45, 37G35, 37H15, 68T01 **DOI:** 10.23939/mmc2025.04.1367

1. Introduction

The memristor, an abbreviated form of "memory resistor", represents a passive circuit component with two terminals whose resistive properties change in response to charge flux. Originally theorized by Leon Chua in 1971 as the fourth elementary circuit component [1], this concept remained in the theoretical domain until its physical realization was demonstrated by researchers at Hewlett-Packard in 2008 [2]. Since then, researchers from numerous scientific and engineering disciplines have focused extensively on memristive devices. The relatively simple architecture of memristive elements and their technological compatibility with complementary metal-oxide-semiconductor (CMOS) fabrication processes enable streamlined integration into existing manufacturing workflows, consequently broadening their spectrum of viable applications [3]. In addition to their compact footprint and minimal power consumption characteristics, memristive devices exhibit a unique memory retention capability specifically, the capacity to preserve information regarding the cumulative charge transport through dynamic resistance modulation. This intrinsic property renders them particularly advantageous for implementation in microprocessor-integrated storage systems [4] and diverse nonvolatile memory architectures [5]. Moreover, memristive components have received considerable attention in the context of hyperchaotic dynamical systems (see [6] and references therein) and neuromorphic computing frameworks, especially as synthetic synaptic elements in artificial neural network architectures [7].

Their ability to replicate synaptic mechanisms observed in biological neural systems positions them as prospective building blocks for constructing brain-inspired computational architectures [8]. Within this framework, memristor-based Hopfield neural networks (MHNNs) have garnered substantial research interest, as evidenced by multiple comprehensive reviews published recently [9, 10]. In contrast to the conventional Hopfield neural network paradigm, the current investigation examines an alternative well-established network topology characterized by the activation function $f_i(z) = \tanh(a_{ij}z_j - \theta_i)$, described by the following differential equation system [11]:

$$\frac{dx_i}{dt} = -b_i x_i + \tanh \sum_{j=1, j\neq i}^{N} a_{ij}x_j + I_i, \tag{1}$$

where x_i denotes the activation state of the i-th neuron, b_i corresponds to the damping coefficient, a_{ij} represent the synaptic coupling strengths, and $I_i(t)$ signifies the external stimulus applied to the i-th neuron.

Sprott [12] established that system (1) is capable of generating diverse dynamical phenomena, including chaotic attractors, via judicious parameterization of the coupling matrix (a_{ij}) and damping vector (b_i), especially when the network dimension (N) is sufficiently large. Additionally, several significant reduced-dimensional configurations were identified in [12,13], which warrant detailed examination:

1. A minimally dissipative neural architecture with $N = 4$, $b = 0.043$;
2. A minimally conservative neural architecture with $N = 4$, $b = 0$;
3. A minimally circulant neural architecture with $N = 5$, $b = 0.12$.

The utilization of system (1) for representing genetic and neural network dynamics in two- and three-dimensional configurations, characterized by non-unity weight parameters, was examined by Samuilik et al. [14,15]. Following these initial investigations, research efforts have progressed toward analyzing Sprott-type artificial neural networks (ANNs) in higher-dimensional phase spaces extending beyond the initial four-dimensional formulation. In particular, Kopp and Samuilik performed comprehensive analyses of five-dimensional (5D) ANN structure [16] and investigated memristor-integrated Sprott system [17], uncovering the manifestation of intricate chaotic phenomena and establishing the presence of rich nonlinear dynamical behavior characteristic of these augmented network configurations

We develop a new five-dimensional neural network framework integrated with a single flux-controlled memristor to simulate the influence of ambient electromagnetic radiation acting on the first neuron.

2. Derivation of a new memristive neural network

A five-dimensional (5D) ANN model was introduced in studies [16,18], expressed in the following form:

$$\begin{cases} \dfrac{dx_1}{dt} = \tanh(x_4 - x_2) - bx_1, \\ \dfrac{dx_2}{dt} = \tanh(x_1 + x_4) - bx_2, \\ \dfrac{dx_3}{dt} = \tanh(x_1 + x_2 - x_4) - bx_3, \\ \dfrac{dx_4}{dt} = \tanh(x_3 - x_2) - bx_4, \\ \dfrac{dx_5}{dt} = \tanh(x_1 + x_4 - x_5) - bx_5, \end{cases} \tag{2}$$

with initial conditions

$$x_1(0) = 1.2, \quad x_2(0) = 0.4, \quad x_3(0) = 1.2, \quad x_4(0) = -1, \quad x_5(0) = -1.$$

Here, b is a parameter governing the rate of dissipation within the system. As established in [16], parametric variation of b induces diverse dynamical regimes in system (2), encompassing equilibrium states, limit cycles, and chaotic attractors. For the parameter $b = 0.043$ and initial conditions $(x_1(0), x_2(0), x_3(0), x_4(0), x_5(0)) = (1.2, 0.4, 1.2, -1, -1)$, the system displays a chaotic attractor. The Lyapunov exponents (LE_i, $i = 1, 2, 3, 4, 5$), along with the Kaplan–Yorke dimension D_{KY}, were also computed as follows [16]:

$$LE_i = (0.035, 0, -0.085, -0.126, -0.697), \quad D_{KY} = 2.488.$$

Advancements in electronic device technology have substantially increased the incidence of electromagnetic radiation exposure in human populations. According to Maxwell's fundamental equations, electromagnetic radiation effects on neuronal units manifest as perturbations in the magnetic flux distribution across membrane surfaces. This flux-voltage relationship can be efficiently represented via a flux-controlled memristive component (refer to [19]). We analyze a neural configuration comprising

five coupled neurons, where the primary neuron undergoes external electromagnetic radiation (EMR) stimulation, as illustrated in Figure 1. The flux-controlled memristor dynamics are mathematically formulated in [20] as:

$$\begin{cases} i_m = W(\varphi)u_m, \\ \dfrac{d\varphi}{dt} = u_m - \mu\varphi, \\ W(\varphi) = \alpha + \beta\varphi^2, \end{cases} \tag{3}$$

where i_m signifies the current flowing through the memristor, u_m denotes the voltage across the memristor, φ is the internal flux, $W(\varphi)$ represents the memductance, and α, β, μ are positive parameters. To illustrate the fundamental characteristics of the memristor described in equation (3), a sinusoidal voltage source $u_m = A\sin(2\pi ft)$ is applied as the input, where A and f represent the amplitude and frequency of the external signal, respectively. The simulation results of the memristor circuit are presented in Figure 2. Under sinusoidal excitation by an alternating current, the current–voltage characteristic of the memristor exhibits a closed hysteresis loop that passes through the origin. As the frequency f increases, the area enclosed by the hysteresis loop gradually decreases, while an increase in amplitude A leads to an expansion of the loop.

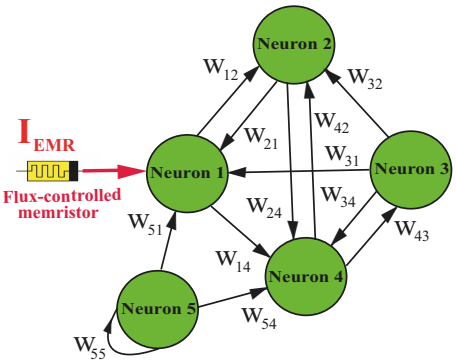

Fig. 1. Connection structure of a five-dimensional memristive artificial neural network. The connection weights are $w_{12} = -1$, $w_{14} = 1$, $w_{21} = 1$, $w_{24} = 1$, $w_{31} = 1$, $w_{32} = 1$, $w_{34} = -1$, $w_{42} = -1$, $w_{43} = 1$, $w_{51} = 1$, $w_{54} = 1$, $w_{55} = -1$.

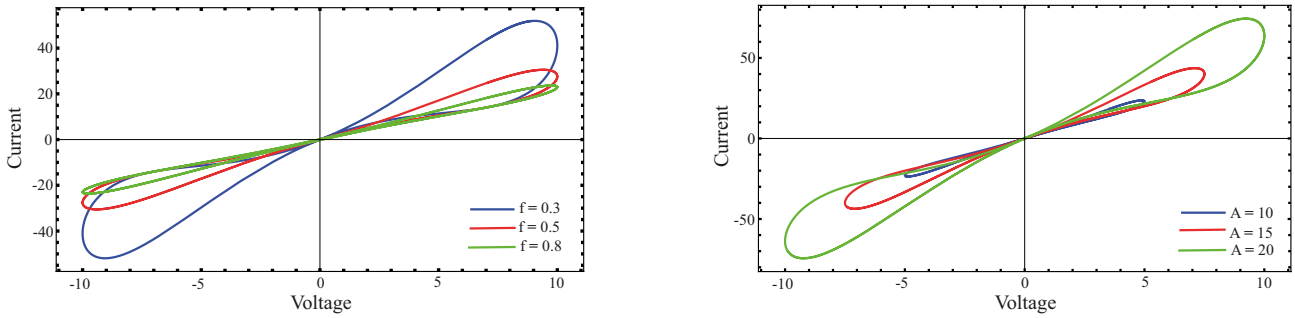

a ***b***

Fig. 2. Simulation of the hysteresis loop of a flux-controlled memristor: (***a***) different values of frequency f; (***b***) different amplitude values A.

Subsequently, the memductance function of the memristive element, as specified by (3), is integrated into the dynamical equation governing neuron 1 to model the electromagnetic radiation effects on that particular neuronal unit. As a result, the governing equations of the neural network system, initially presented in (2), are reformulated as:

$$\begin{cases} \dfrac{dx_1}{dt} = \tanh(x_4 - x_2) - bx_1 - \beta\varphi^2 x_1, \\ \dfrac{dx_2}{dt} = \tanh(x_1 + x_4) - bx_2, \\ \dfrac{dx_3}{dt} = \tanh(x_1 + x_2 - x_4) - bx_3, \\ \dfrac{dx_4}{dt} = \tanh(x_3 - x_2) - bx_4, \\ \dfrac{dx_5}{dt} = \tanh(x_1 + x_4 - x_5) - bx_5, \\ \dfrac{d\varphi}{dt} = x_1 - \mu\varphi. \end{cases} \tag{4}$$

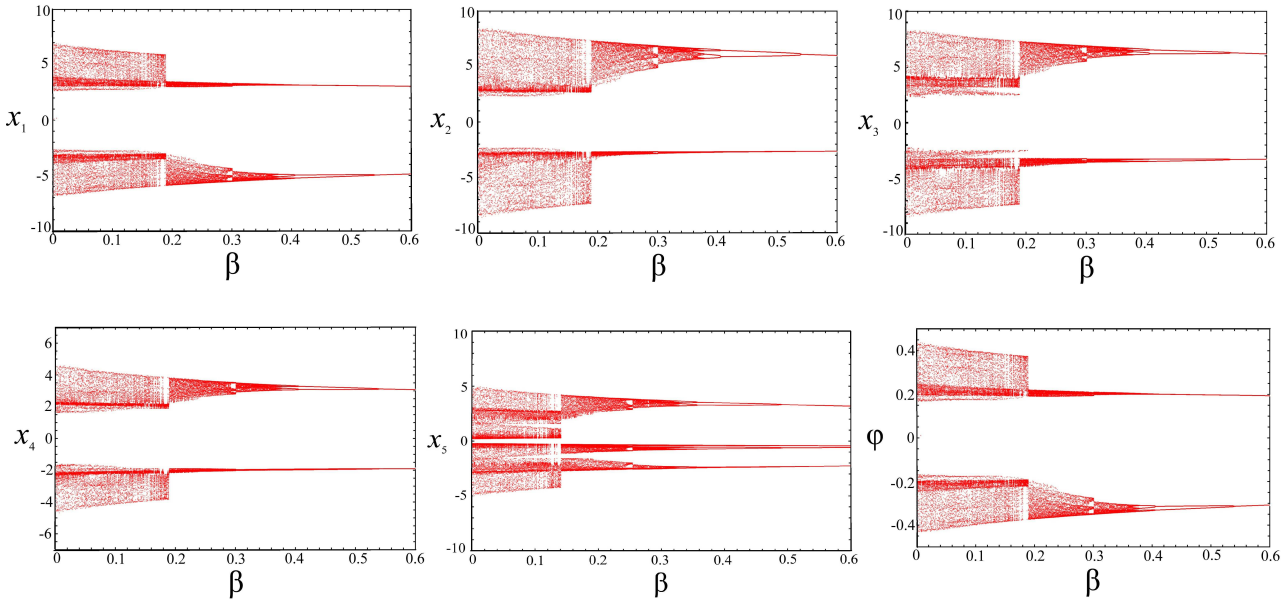

Fig. 3. Bifurcation diagrams for x_1, x_2, x_3, x_4, x_5, φ components of the system (4) with variations of the parameter β.

In the modified system (4), the parameters β and μ serve distinct roles: β represents the feedback intensity of the electromagnetic radiation, while μ quantifies the effect of magnetic flux on the generation of the membrane potential x_1. The term φ^2 corresponds to the memductance of the flux-controlled memristor, capturing the nonlinear coupling between the magnetic flux φ and the membrane voltage. Based on the functional characteristics of flux-controlled memristors, the impact of external electromagnetic radiation on the neuron can be effectively modeled as an additional excitation current, expressed as $I_{\text{EMR}} = \beta\varphi^2 x_1$. System (3) is supplemented with initial conditions:

$$(x_1(0), x_2(0), x_3(0), x_4(0), x_5(0), \varphi(0)) = (1.2, 0.4, 1.2, -1, -1, 1.2). \tag{5}$$

It is important to note that the proposed memristive neural network can be controlled by three key parameters: b, β, and μ. It is straightforward to observe that system (4) remains invariant under the transformation: $\mathbf{T}$: $(x_1, x_2, x_3, x_4, x_5, \varphi) \to (-x_1, -x_2, -x_3, -x_4, -x_5, -\varphi)$. By computing the divergence of the vector field $\mathbf{\Phi} = (\dot{x}_1, \dot{x}_2, \dot{x}_3, \dot{x}_4, \dot{x}_5, \dot{\varphi})$:

$$\text{div}\mathbf{\Phi} = \frac{\partial \dot{x}_1}{\partial x_1} + \frac{\partial \dot{x}_2}{\partial x_2} + \frac{\partial \dot{x}_3}{\partial x_3} + \frac{\partial \dot{x}_4}{\partial x_4} + \frac{\partial \dot{x}_5}{\partial x_5} + \frac{\partial \dot{\varphi}}{\partial \varphi} = -(5b + \beta\varphi^2 + \mu + 1) + \tanh^2(x_1 + x_4 - x_5).$$

The system (4) exhibits dissipative behavior since the divergence of the vector field is negative for all positive parameters $b > 0$, $\mu > 0$, and $\beta > 0$. This property is necessary for the existence of a chaotic attractor.

3. Dynamical analysis and numerical simulation

This section examines the dynamical properties of the proposed memristive neural network using both analytical and numerical approaches. The nonlinear dynamics are characterized through several computational techniques, including bifurcation diagrams, Lyapunov exponent spectra, Kaplan–Yorke dimension calculations, temporal evolution analysis, and phase space representation.

3.1. Bifurcation diagrams, Lyapunov exponents and Kaplan–Yorke dimension

Bifurcation diagrams are constructed numerically in Mathematica using system (4) and initial conditions (5) to characterize the parameter-dependent dynamics. Figure 3 presents the bifurcation structure versus the memristor coupling parameter β for fixed $b = 0.043$ and $\mu = 15.8$, while Figure 4 shows the corresponding behavior versus the magnetic flux parameter μ with $\beta = 0.1$ and $b = 0.043$. Both diagrams exhibit well-defined regions of periodic, quasi-periodic, and chaotic dynamics. Regime identi-

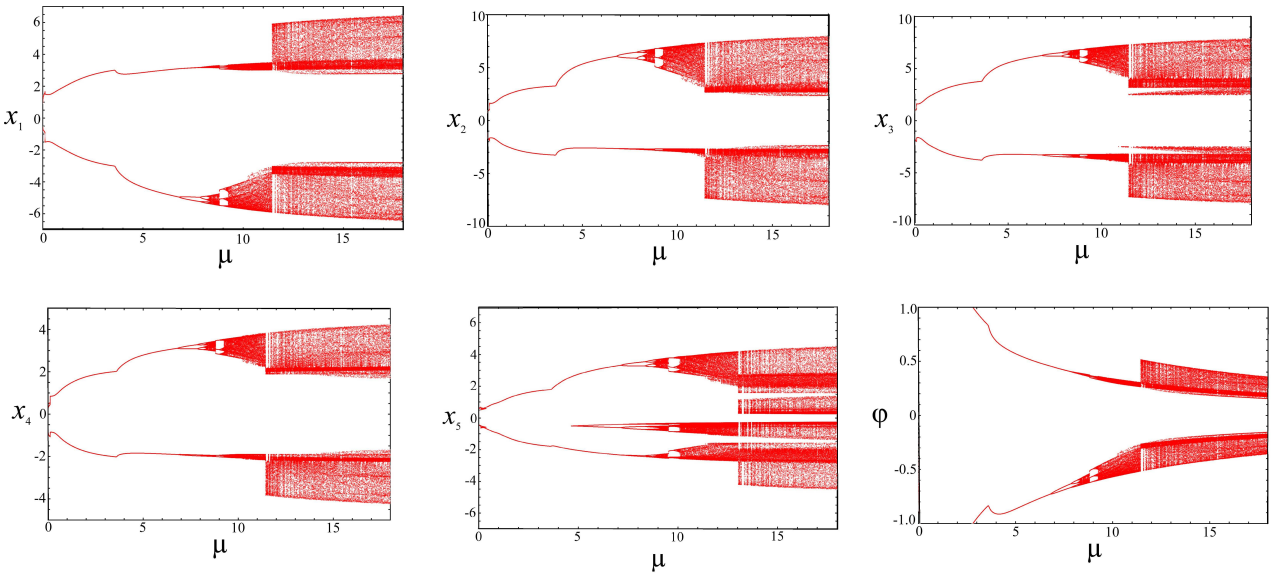

Fig. 4. Bifurcation diagrams for x_1, x_2, x_3, x_4, x_5, φ components of the system (4) with variations of the parameter μ.

fication is performed through combined qualitative-quantitative analysis: periodic orbits correspond to discrete points in the bifurcation diagram and negative Lyapunov exponents; quasi-periodic solutions appear as continuous bands with zero maximum Lyapunov exponent; chaotic attractors manifest as scattered distributions with positive Lyapunov exponents, reflecting sensitivity to initial conditions.

In this study, the Lyapunov exponents were computed using the Benettin–Wolfe algorithm [21,22], along with the numerical approaches proposed by Binous et al. [23] and Sandri [24], implemented in the Mathematica environment. The complete set of Lyapunov exponents for the proposed memristive Sprott system (3), under the initial conditions (4) and parameter values

$$b = 0.043, \quad \beta = 0.1, \quad \mu = 15.8, \tag{6}$$

is obtained as follows:

$$LE_1 = 0.02952, \qquad LE_2 = 0.00434 \approx 0, \qquad LE_3 = -0.07879,$$
$$LE_4 = -0.1338, \qquad LE_5 = -0.7809, \qquad LE_6 = -15.8002.$$

The existence of a positive Lyapunov exponent LE_1 confirms the presence of chaotic dynamics in system (4). Additionally, the negative sum of the Lyapunov exponents, $\sum_{i=1}^{5} LE_i = -16.7599 < 0$, reveals the dissipative nature of the system, indicating that the phase space volume continuously contracts over time – a hallmark of chaotic yet bounded behavior. To further quantify the complexity of the resulting attractor, the Lyapunov (Kaplan–Yorke) dimension is evaluated using the method outlined in Ref. [25] in the following form:

$$D_{KY} = \xi + \frac{1}{|LE_{\xi+1}|}\sum_{i=1}^{\xi} LE_i = 2 + \frac{0.03382}{0.07879} \approx 2.430,$$

where ξ is determined from the conditions

$$\sum_{i=1}^{\xi} LE_i > 0 \quad \Rightarrow \quad \sum_{i=1}^{2} LE_i = 0.03382.$$

Here, ξ denotes the number of the largest consecutive non-negative Lyapunov exponents in the spectrum. The Kaplan–Yorke (or Lyapunov) dimension provides an estimate of the fractal dimensionality of a strange attractor, serving as a quantitative indicator of the system's dynamic complexity. Figure 5 illustrates the evolution of the Lyapunov exponents, as defined by expression (6).

A detailed visual examination of the chaotic attractor is carried out through phase portrait analysis. Next, instead of representing the magnetic flux with the symbol φ, we introduce a new dynamical variable x_6. Utilizing Mathematica, we generated phase portraits in the projection planes x_1x_3, x_2x_4,

x_3x_5, x_3x_6, x_4x_5 and x_5x_6, alongside the time series of the state variables for the chaotic system (4), as depicted in Figure 6. The temporal evolution of the components $x_1, x_2, x_3, x_4, x_5, x_6$ reveals an aperiodic structure, which is a hallmark of chaotic dynamics. Furthermore, as shown in Figure 7, all dynamic variables x_i remain confined within the power supply limits of the operational amplifiers (± 15 V), ensuring the system's feasibility for analog circuit implementation.

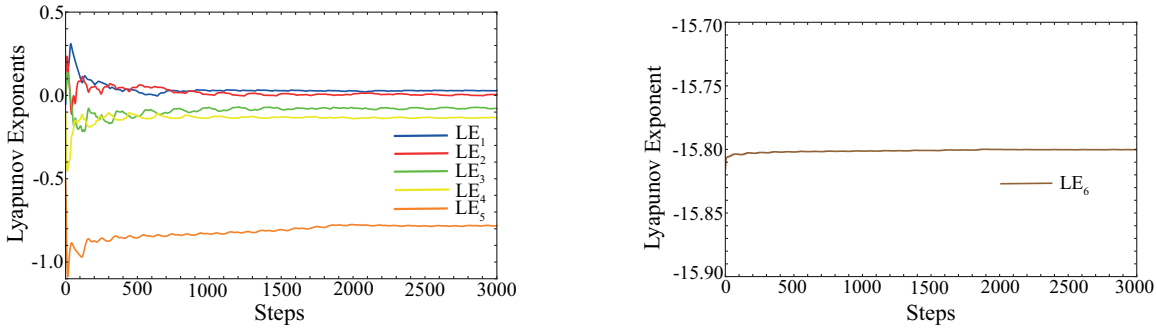

Fig. 5. The convergence plot of the Lyapunov spectrum for the system (4).

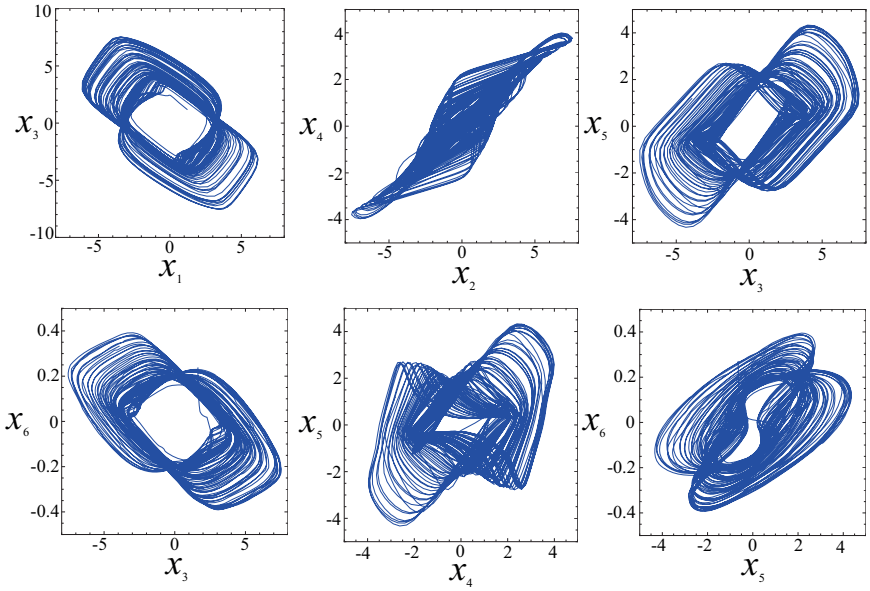

Fig. 6. Chaotic attractors of the system (4) in various planes.

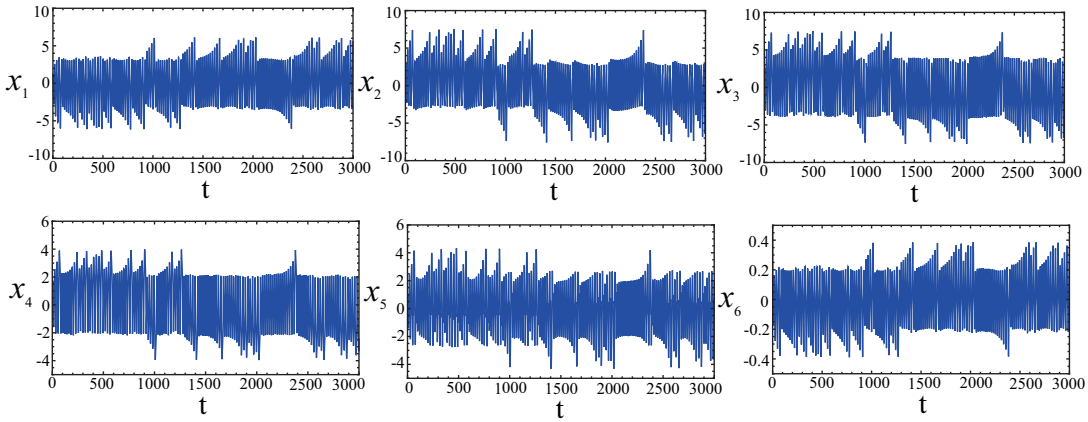

Fig. 7. Time diagrams for variables $x_1, x_2, x_3, x_4, x_5, x_6$ ($x_6 = \varphi$) of the system (4).

3.2. Analysis of equilibrium points and their stability

To determine the equilibrium points of system (3), we set $\dot{x}_i = 0$ for $i = (1, 2, 3, 4, 5, 6)$, yielding the following algebraic conditions:

$$\begin{cases} 0 = \tanh(\widetilde{x}_4 - \widetilde{x}_2) - b\widetilde{x}_1 - \beta\widetilde{x}_6^2\widetilde{x}_1, \\ 0 = \tanh(\widetilde{x}_1 + \widetilde{x}_4) - b\widetilde{x}_2, \\ 0 = \tanh(\widetilde{x}_1 + \widetilde{x}_2 - \widetilde{x}_4) - b\widetilde{x}_3, \\ 0 = \tanh(\widetilde{x}_3 - \widetilde{x}_2) - b\widetilde{x}_4, \\ 0 = \tanh(\widetilde{x}_1 + \widetilde{x}_4 - \widetilde{x}_5) - b\widetilde{x}_5, \\ 0 = \widetilde{x}_1 - \mu\widetilde{x}_6. \end{cases} \tag{7}$$

The last equation of system (7) immediately yields the equality $\widetilde{x}_6 = \widetilde{x}_1/\mu$. It is evident that system (7) constitutes a set of transcendental equations of fifth order, rendering an analytical solution highly nontrivial. Consequently, numerical methods are employed to compute the equilibrium points. We concluded that system (7) possesses a single equilibrium point, denoted as $E(0, 0, 0, 0, 0, 0)$. The stability of equilibrium point is determined from the analysis of the eigenvalues (λ_i) of the Jacobian matrix of the following form:

$$J(E) = \begin{vmatrix} -b - \beta\widetilde{x}_6^2 & -g_1 & 0 & g_1 & 0 & -2\beta\widetilde{x}_1\widetilde{x}_6 \\ g_2 & -b & 0 & g_2 & 0 & 0 \\ g_3 & g_3 & -b & -g_3 & 0 & 0 \\ 0 & -g_4 & g_4 & -b & 0 & 0 \\ g_5 & 0 & 0 & g_5 & -g_5 - b & 0 \\ 1 & 0 & 0 & 0 & 0 & -\mu \end{vmatrix},$$

where

$$g_1 = \frac{4\mathrm{e}^{-2(\widetilde{x}_4 - \widetilde{x}_2)}}{\left(1 + \mathrm{e}^{-2(\widetilde{x}_4 - \widetilde{x}_2)}\right)^2}, \quad g_2 = \frac{4\mathrm{e}^{-2(\widetilde{x}_1 + \widetilde{x}_4)}}{\left(1 + \mathrm{e}^{-2(\widetilde{x}_1 + \widetilde{x}_4)}\right)^2}, \quad g_3 = \frac{4\mathrm{e}^{-2(\widetilde{x}_1 + \widetilde{x}_2 - \widetilde{x}_4)}}{\left(1 + \mathrm{e}^{-2(\widetilde{x}_1 + \widetilde{x}_2 - \widetilde{x}_4)}\right)^2},$$

$$g_4 = \frac{4\mathrm{e}^{-2(\widetilde{x}_3 - \widetilde{x}_2)}}{\left(1 + \mathrm{e}^{-2(\widetilde{x}_3 - \widetilde{x}_2)}\right)^2}, \quad g_5 = \frac{4\mathrm{e}^{-2(\widetilde{x}_1 + \widetilde{x}_4 - \widetilde{x}_5)}}{\left(1 + \mathrm{e}^{-2(\widetilde{x}_1 + \widetilde{x}_4 - \widetilde{x}_5)}\right)^2}.$$

Jacobian matrix was obtained by linearizing the system of equations (4) around the set of equilibria: $(\widetilde{x}_i)$. The characteristic polynomial at the equilibrium point $E(0, 0, 0, 0, 0, 0)$ and parameter values (6) is expressed as

$$\begin{aligned} P(\lambda) &= a_0\lambda^6 + a_1\lambda^5 + a_2\lambda^4 + a_3\lambda^3 + a_2\lambda^2 + a_1\lambda + a_6 \\ &= \lambda^6 + 17.015\lambda^5 + 22.387\lambda^4 + 52.808\lambda^3 + 38.091\lambda^2 + 3.989\lambda + 15.862. \end{aligned} \tag{8}$$

Analyzing the coefficients a_i and apply the Routh–Hurwitz criterion can provide insights into the stability and dynamics of the system near the equilibrium point. The principal minors of the Hurwitz matrix associated with the characteristic equation (8) are given as follows:

$$\begin{aligned} &\Delta_1 = a_1 = 17.015 > 0, \quad \Delta_2 = -a_0a_3 + a_1a_2 = 328.106 > 0, \\ &\Delta_3 = a_3\Delta_2 - a_1(-a_0a_5 + a_1a_4) = 6366.803 > 0, \\ &\Delta_4 = a_4\Delta_3 - a_5(a_2\Delta_2 - a_0(a_1a_4 - a_1a_5)) + a_6(-a_0a_1a_3 + a_1^2a_2) = 3.040 \cdot 10^5 > 0, \\ &\Delta_5 = a_5\Delta_4 - a_6a_3\Delta_3 - a_1a_6(-a_1^2a_6 + a_5\Delta_3) = -9.735 \cdot 10^6 < 0, \quad \Delta_6 = a_1\Delta_5 = -1.656 \cdot 10^8. \end{aligned} \tag{9}$$

From expressions (9), it is evident that not all principal minors of the Hurwitz determinant are positive, indicating that the system is unstable. This conclusion is further supported by the numerical solution of the characteristic equation (8), which reveals the existence of roots with positive real parts:

$$\lambda_1 = -1.043, \quad \lambda_2 = -15.8, \quad \lambda_{3,4} = 0.161 \pm i0.561, \quad \lambda_{5,6} = -0.247 \pm i1.664.$$

The presence of a positive real part in the complex conjugate roots $\lambda_{3,4}$ characterizes the system as a saddle-focus type, confirming the instability of system (4). This instability implies the existence of a self-excited attractor.

4. Electronic circuit implementation

The analog implementation of neurons and neural networks presents significant potential for artificial intelligence applications, particularly in domains demanding high-speed parallel computation and energy-efficient operation. The electronic circuit described herein employs standard, commercially available components including resistors, capacitors, analog multipliers, diodes, and operational amplifiers sourced from the Multisim simulation library. In the proposed analog realization, the state variables of the dynamical system (4) are mapped to electrical signals represented by the instantaneous voltages across capacitors C_1, C_2, C_3, C_4, C_5, C_6, designated as $U_1(\tau)$, $U_2(\tau)$, $U_3(\tau)$, $U_4(\tau)$, $U_5(\tau)$, $U_6(\tau)$, respectively. Through the application of Kirchhoff's circuit laws, an electrical analog of system (4) is established, resulting in a system of coupled differential equations that characterize the circuit dynamics:

$$\begin{cases} C_1\dfrac{dU_1}{d\tau} = -\dfrac{U_1}{R_{11}} + \dfrac{1}{R_{12}}\tanh(U_4 - U_2) - \dfrac{U_6^2 U_1}{R_{13}\cdot K^2}, \\ C_2\dfrac{dU_2}{d\tau} = -\dfrac{U_2}{R_{21}} + \dfrac{1}{R_{22}}\tanh(U_1 + U_4), \\ C_3\dfrac{dU_3}{d\tau} = -\dfrac{U_3}{R_{31}} + \dfrac{1}{R_{32}}\tanh(U_1 + U_2 - U_4), \\ C_4\dfrac{dU_4}{d\tau} = -\dfrac{U_4}{R_{41}} + \dfrac{1}{R_{42}}\tanh(U_3 - U_2), \\ C_5\dfrac{dU_5}{d\tau} = -\dfrac{U_5}{R_{51}} + \dfrac{1}{R_{52}}\tanh(U_1 + U_4 - U_5), \\ C_6\dfrac{dU_6}{d\tau} = -\dfrac{U_6}{R_{61}} + \dfrac{U_1}{R_{62}}, \end{cases} \tag{10}$$

where R_{ij} represent resistors $(i,j) = \{1,2,3,4,5,6\}$, and K is a scaling coefficient for the multiplier. We normalize the resistor as $R_0 = 100\,\text{k}\Omega$ and the capacitor as $C_0 = 0.15\,\text{nF}$, giving a time constant of $t_0 = R_0C_0 = 1.5\cdot 10^{-5}\,\text{s}$. The state variables of the system (10) are rescaled as follows: $U_1 = U_0\widetilde{X}_1$, $U_2 = U_0\widetilde{X}_2$, $U_3 = U_0\widetilde{X}_3$, $U_4 = U_0\widetilde{X}_4$, $U_5 = U_0\widetilde{X}_5$, $U_6 = U_0\widetilde{X}_6$, $K = U_0K'$, and $\tau = t_0 t$. By substituting R_0, $C_1 = C_2 = C_3 = C_4 = C_5 = C_6 = C_0$ and $K' = 10$ into system (10) and comparing the numerical values of the output voltages in (10) and (4) for the parameter values (5), we determine the values of the electronic circuit resistors as follows:

$$\begin{cases} \dfrac{d\widetilde{X}_1}{d\tau} = -\dfrac{100\text{k}}{R_1}\widetilde{X}_1 + \dfrac{100\text{k}}{R_2}\tanh(\widetilde{X}_4 - \widetilde{X}_2) - \dfrac{100\text{k}}{R_3}\dfrac{\widetilde{X}_6^2\widetilde{X}_1}{K'^2}, \\ \dfrac{d\widetilde{X}_2}{d\tau} = -\dfrac{100\text{k}}{R_4}\widetilde{X}_2 + \dfrac{100\text{k}}{R_5}\tanh(\widetilde{X}_1 + \widetilde{X}_4), \\ \dfrac{d\widetilde{X}_3}{d\tau} = -\dfrac{100\text{k}}{R_6}\widetilde{X}_3 + \dfrac{100\text{k}}{R_7}\tanh(\widetilde{X}_1 + \widetilde{X}_2 - \widetilde{X}_4), \\ \dfrac{d\widetilde{X}_4}{d\tau} = -\dfrac{100\text{k}}{R_8}\widetilde{X}_4 + \dfrac{100\text{k}}{R_9}\tanh(\widetilde{X}_3 - \widetilde{X}_2), \\ \dfrac{d\widetilde{X}_5}{d\tau} = -\dfrac{100\text{k}}{R_{10}}\widetilde{X}_5 + \dfrac{100\text{k}}{R_{11}}\tanh(\widetilde{X}_1 + \widetilde{X}_4 - \widetilde{X}_5), \\ \dfrac{d\widetilde{X}_6}{d\tau} = -\dfrac{100\text{k}}{R_{12}}\widetilde{X}_6 + \dfrac{100\text{k}}{R_{13}}\widetilde{X}_1, \end{cases} \tag{11}$$

where

$$R_1 = R_4 = R_6 = R_8 = R_{10} = 2.325\ \text{M}\Omega,$$
$$R_2 = R_5 = R_7 = R_9 = R_{11} = R_{13} = 100\ \text{k}\Omega,$$
$$R_3 = 10\ \text{k}\Omega, \quad R_{12} = 6.329\ \text{k}\Omega.$$

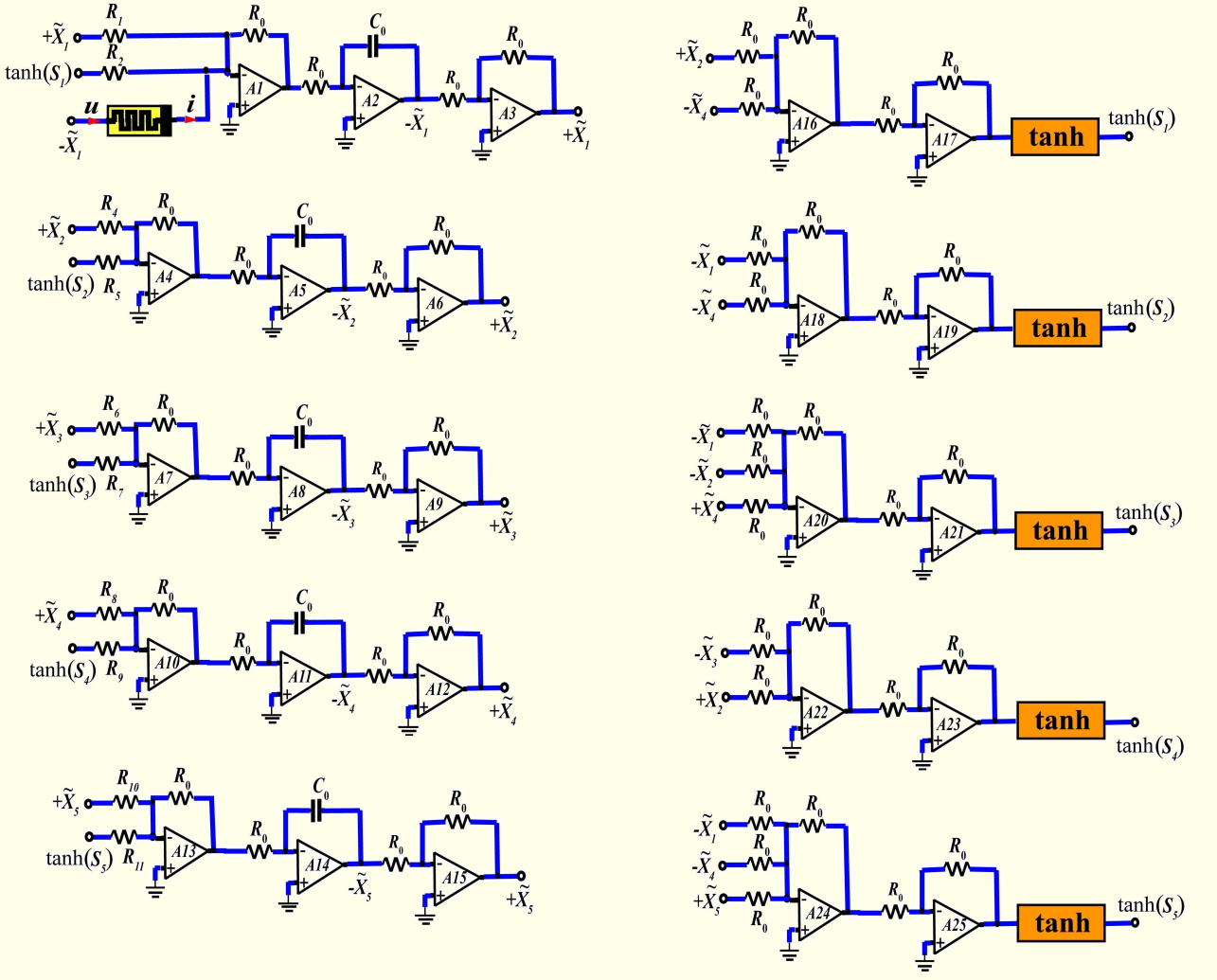

Fig. 8. Circuit modules implemented based on a system of equations (11).

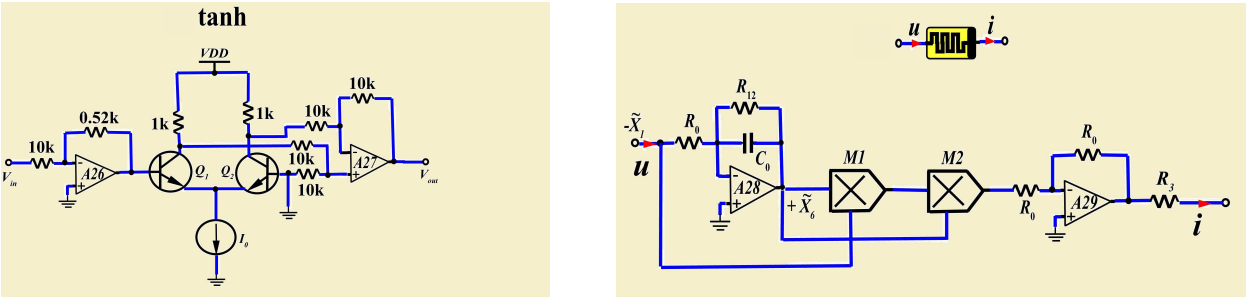

a *b*

Fig. 9. The circuit scheme includes two components: (***a***) the hyperbolic tangent function and (***b***) the memristor emulator.

Figure 8 presents the analog circuit modules that correspond to the differential equations of system (11). These modules are implemented using standard electronic components, including resistors (R), capacitors (C), analog multipliers (M1-M2), operational amplifiers (A1–A29, TL084ACN), and a power supply of $\pm 15\,\mathrm{V}$.

Figure 9 illustrates the specialized circuit blocks designed to emulate the hyperbolic tangent function and the flux-controlled memristor. As shown, the hyperbolic tangent function is realized using two MPS2222 transistors (Q1 and Q2), two TL084ACN operational amplifiers, and a constant current source ($I_0 = 1.1\,\mathrm{mA}$).

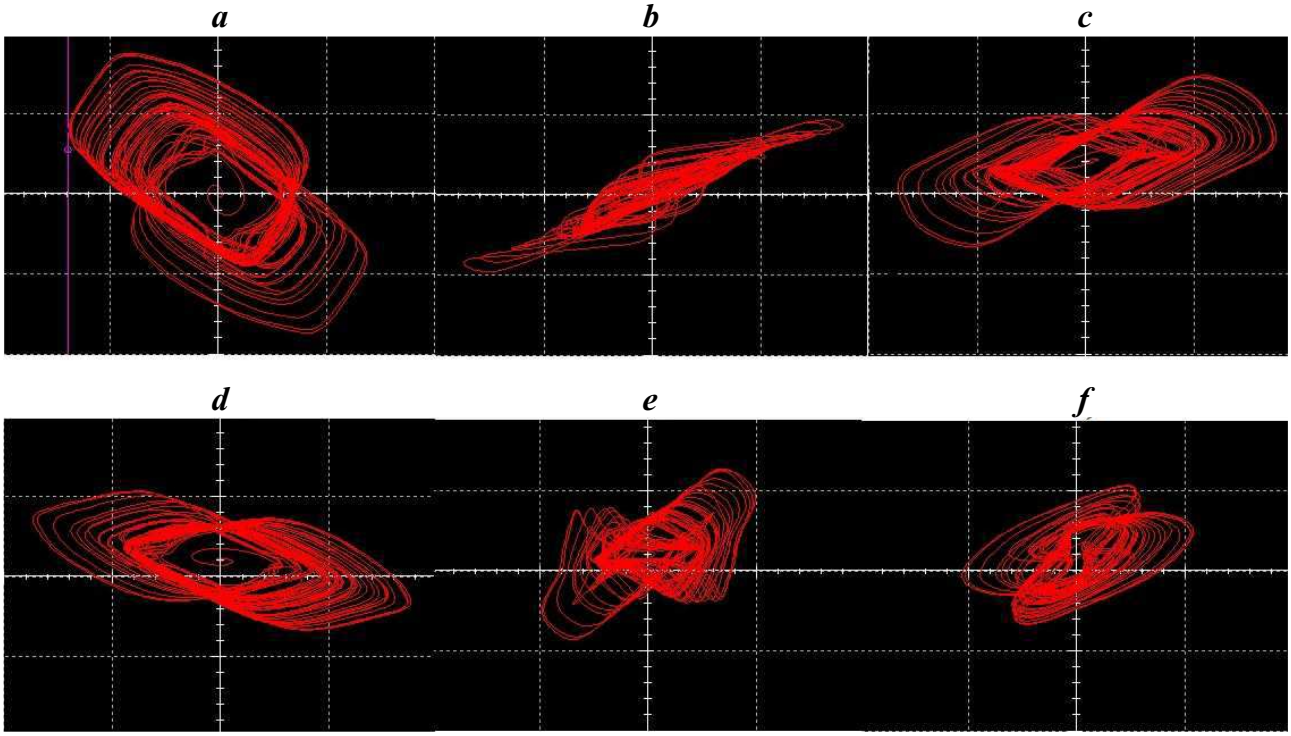

Fig. 10. Phase portraits of the system (11) as generated in Multisim oscilloscopes: (***a***) $\widetilde{X}_1\widetilde{X}_3$, (***b***) $\widetilde{X}_2\widetilde{X}_4$, (***c***) $\widetilde{X}_3\widetilde{X}_5$, (***d***) $\widetilde{X}_3\widetilde{X}_6$, (***e***) $\widetilde{X}_4\widetilde{X}_5$, (***f***) $\widetilde{X}_5\widetilde{X}_6$.

The results of the circuit simulation, shown in Figure 10, exhibit excellent agreement with the numerical simulations carried out in Mathematica (see Figure 6), thereby validating the proposed analog implementation.

5. Synchronization in the coupling subnetworks

Synchronization represents a fundamental phenomenon in memristive neural networks, particularly those designed to capture the complex dynamics observed in biological neural systems. In the human brain, synchronized electrical activity across distinct regions is essential for coherent cognitive function, facilitating efficient information processing and transmission. This neural coordination emerges through interregional connectivity, where neurons interact via synaptic pathways. Inspired by this biological principle, we examine the synchronization dynamics between two coupled memristive subnetworks, each described by the six-dimensional dynamical model presented in equation (4). The two subnetworks are interconnected through a synaptic coupling mediated by a single neuron. Let $(x_1, x_2, x_3, x_4, x_5, x_6)$ and $(y_1, y_2, y_3, y_4, y_5, y_6)$ denote the state variables of the first and second subnetworks, respectively, where $x_6 = \phi_1$ and $y_6 = \phi_2$ represent the magnetic flux states of the memristors in each subnetwork. The interaction between these subnetworks is modeled through synaptic coupling, and the corresponding mathematical formulation of the coupled system is given by:

$$\begin{cases} \dfrac{dx_1}{dt} = \tanh(x_4 - x_2) - bx_1 - \beta x_6^2 x_1 + p(x_1 - y_1), \\ \dfrac{dx_2}{dt} = \tanh(x_1 + x_4) - bx_2, \\ \dfrac{dx_3}{dt} = \tanh(x_1 + x_2 - x_4) - bx_3, \\ \dfrac{dx_4}{dt} = \tanh(x_3 - x_2) - bx_4, \\ \dfrac{dx_5}{dt} = \tanh(x_1 + x_4 - x_5) - bx_5, \\ \dfrac{dx_6}{dt} = x_1 - \mu x_6, \\ \dfrac{dy_1}{dt} = \tanh(y_4 - y_2) - by_1 - \beta y_6^2 y_1 - p(x_1 - y_1), \\ \dfrac{dy_2}{dt} = \tanh(y_1 + y_4) - by_2, \\ \dfrac{dy_3}{dt} = \tanh(y_1 + y_2 - y_4) - by_3, \\ \dfrac{dy_4}{dt} = \tanh(y_3 - y_2) - by_4, \\ \dfrac{dy_5}{dt} = \tanh(y_1 + y_4 - y_5) - by_5, \\ \dfrac{dy_6}{dt} = y_1 - \mu y_6, \end{cases} \tag{12}$$

where p represents the synaptic coupling strength of the sub-neural networks. Complete synchronization of the coupled neural network described by equation (12) occurs when the state trajectories of the two subnetworks asymptotically converge to identical dynamics. Mathematically, this condition is satisfied if $e_i = |x_i(t) - y_i(t)|_{t\to\infty} \to 0$, for $i = (1, 2, 3, 4, 5, 6)$. Then the system (12) gives rise to the following error e_i dynamics system:

$$\begin{cases} \dfrac{de_1}{dt} = \tanh(x_4 - x_2) - \tanh(y_4 - y_2) - be_1 - \beta(x_6^2 x_1 - y_6^2 y_1) + 2p\, e_1, \\ \dfrac{de_2}{dt} = \tanh(x_1 + x_4) - \tanh(y_1 + y_4) - e_2, \\ \dfrac{de_3}{dt} = \tanh(x_1 + x_2 - x_4) - \tanh(y_1 + y_2 - y_4) - be_3, \\ \dfrac{de_4}{dt} = \tanh(x_3 - x_2) - \tanh(y_3 - y_2) - be_4, \\ \dfrac{de_5}{dt} = \tanh(x_1 + x_4 - x_5) - \tanh(y_1 + y_4 - y_5) - be_5, \\ \dfrac{de_6}{dt} = e_1 - \mu e_6. \end{cases} \tag{13}$$

Equations (12) and (13) were integrated using the Runge–Kutta–Felberg method ($rkf45$) implemented in the Maple computing environment. The analysis was performed with fixed system parameters specified in (6), with different initial conditions (ICs) assigned to each subnetwork, as follows:

$$(x_1(0), x_2(0), x_3(0), x_4(0), x_5(0), x_6(0)) = (1.2001, 0.4001, 1.2001, -1.0001, -1.0001, 1.2001),$$
$$(y_1(0), y_2(0), y_3(0), y_4(0), y_5(0), y_6(0)) = (1.2, 0.4, 1.2, -1, -1, 1.2).$$

For a coupling strength of $p = -0.2$, the numerical simulation results are depicted in Figure 11. As depicted in Figure 11, the synchronization error dynamics reveal a two-phase behavior: an initial transient phase ($t \in [0, 100]$) characterized by near-complete synchronization with minimal error, followed

by a gradual desynchronization phase where the error increases over time. This phenomenon can be attributed to several factors inherent to the memristive system dynamics. First, the accumulation of small numerical errors or intrinsic system noise may destabilize the synchronized state over extended time intervals. Second, the non-ideal nature of the flux-controlled memristor introduces memory-dependent nonlinearities that can cause the coupled subnetworks to diverge from the synchronized manifold. Third, the presence of chaos in the individual subnetworks implies sensitivity to initial conditions, which may manifest as divergence between trajectories despite initial coupling strength. This behavior suggests that the coupling mechanism provides robust short-term synchronization but is insufficient to maintain long-term coherence in the presence of chaotic dynamics. From a biological perspective, this transient synchronization followed by desynchronization mirrors observations in neural systems where synchronized activity patterns are often temporary and task-dependent rather than perpetually stable.

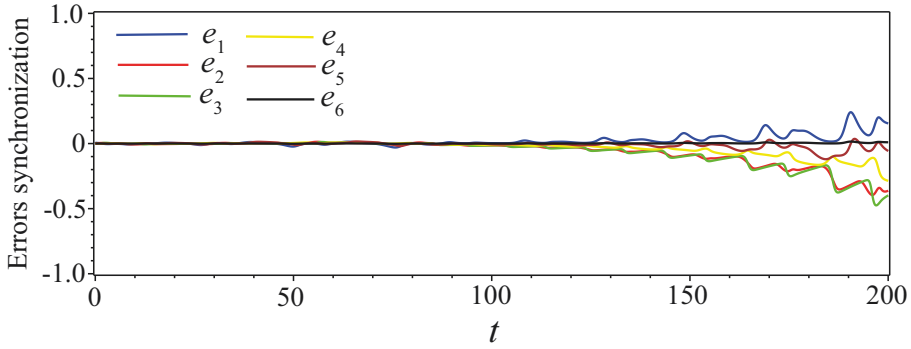

Fig. 11. Errors synchronization of subnetworks over time.

6. Conclusion

This study introduces a novel memristive neural network architecture comprising five neurons coupled with a single non-ideal flux-controlled memristor. The memristor models external electromagnetic radiation effects on the first neuron. A comprehensive dynamical analysis was performed, incorporating bifurcation diagrams as functions of the memristor control parameter and magnetic flux loss parameter. Lyapunov exponents and the Kaplan–Yorke dimension were computed to characterize the identified chaotic attractor. Numerical simulations enabled visualization through phase portraits and temporal evolution diagrams. The chaotic attractor exhibits a markedly negative sixth Lyapunov exponent, indicating strong contraction within the system and confirming its dissipative nature with continuous phase space volume contraction. An analog circuit realization of the proposed six-dimensional memristive system was implemented using standard electronic components in Multisim. The resulting phase portraits showed excellent agreement with numerical simulations in Mathematica, validating the theoretical framework. To investigate synchronization phenomena in biological neural networks, we developed a coupled architecture of two subneural memristive networks. This configuration demonstrates transient synchronization, providing insights into the temporal dynamics of interregional coordination mechanisms underlying brain function.

[1] Chua L. O. Memristor – The missing circuit element. IEEE Transactions on Circuit Theory. **18** (5), 507–519 (1971).

[2] Strukov D. B., Snider G. S., Stewart D. R., Williams R. S. The missing memristor found. Nature. **453**, 80–83 (2008).

[3] Xiao Z., Yan B., Zhang T., Huang R., Yang Y. Memristive devices-based hardware for unlabeled data processing. Neuromorphic Computing and Engineering. **2** (2), 022003 (2022).

[4] Yang J. J., Pickett M. D., Li X., Ohlberg D. A. A., Stewart D. R., Williams R. S. Memristive switching mechanism for metal/oxide/metal nanodevices. Nature Nanotechnology. **3** (7), 429–433 (2008).

[5] Junsangsri P., Lombardi F. Design of a hybrid memory cell using memristance and ambipolarity. IEEE Transactions on Nanotechnology. **12** (1), 71–80 (2013).

[6] Kopp M. I. A New Memristor-Based 4D Hyperchaotic System with Seven Terms and No Equilibrium Points. Nonlinear Dynamics and Systems Theory. **3** (5), 288–298 (2025).

[7] Vaidyanathan S. Adaptive Control of the Fitzhugh-Nagumo Chaotic Neuron Model. International Journal of PharmTech Research. **8** (6), 117–127 (2015).

[8] Choi S., Ham S., Wang G. Memristor Synapses for Neuromorphic Computing, Memristors – Circuits and Applications of Memristor Devices. IntechOpen (2019).

[9] Lin H., Wang C., Deng Q., Xu C., Deng Z., Zhou C. Review on chaotic dynamics of memristive neuron and neural network. Nonlinear Dynamics. **106**, 959–973 (2021).

[10] Lin H., Wang C., Yu F., Sun J., Du S., Deng Z., Deng Q. A Review of Chaotic Systems Based On Memristive Hopfield Neural Networks. Mathematics. **11** (6), 1369 (2023).

[11] Haykin S. Neural Networks: A Comprehensive Foundation. Prentice-Hall, Englewood Cliffs (1998).

[12] Sprott J. C. Chaotic dynamics on large networks. Chaos. **18** (2), 023135 (2008).

[13] Sprott J. C. Elegant Chaos. Algebraically Simple Chaotic Flows. World Scientific Publishing Company (2010).

[14] Samuilik I., Sadyrbaev F., Ogorelova D. Comparative Analysis of Models of Gene and Neural Networks. Contemporary Mathematics. **4** (2), 217–229 (2023).

[15] Ogorelova D., Sadyrbaev F. Remarks on the Mathematical Modeling of Gene and Neuronal Networks by Ordinary Differential Equations. Axioms. **13** (1), 61 (2024).

[16] Kopp M. I., Samuilik I. I. Computer modeling and circuit implementation of a fivedimensional artificial neural network system. X International Scientific-Practical Conference Physical and Technological Problems of Transmission, Processing and Storage of Information in Infocommunication Systems, 15–17 May 2025, Chernivtsi, Ukraine. Book of Abstracts. 92–93 (2025).

[17] Kopp M. I., Samuilik I. Chaotic dynamics in Sprott's memristive artificial neural network: dynamic analysis, circuit implementation and synchronization. AIMS Mathematics. **10** (8), 19240–19266 (2023).

[18] Samuilik I., Sadyrbaev F., Atslega S. On mathematical models of artificial neural networks. Proceedings of 22nd International Scientific Conference Engineering for Rural Development, May 24-26, 45-50 (2023).

[19] Lin H., Wang C., Yao W., Tan Y. Chaotic dynamics in a neural network with different types of external stimuli. Communications in Nonlinear Science and Numerical Simulation. **90**, 105390 (2020).

[20] Sundarapandian V., Volos Ch. Advances in Memristors, Memristive Devices and Systems. Springer, Cham, Switzerland (2017).

[21] Benettin G., Galgani L., Giorgilli A., Strelcyn J.-M. Lyapunov Characteristic Exponents for smooth dynamical systems and for hamiltonian systems; a method for computing all of them. Part 1: Theory. Meccanica. **15**, 9–20 (1980).

[22] Wolf A., Swift J. B., Swinney H. L., Vastano J. A. Determining Lyapunov Exponents from a Time Series. Physica D. **16** (3), 285–317 (1985).

[23] Binous H., Zakia N. An Improved Method for Lyapunov Exponents Computation. `https://library.wolfram.com/infocenter/MathSource/7109/` (2008).

[24] Sandri M. Numerical Calculation of Lyapunov Exponents. The Mathematica Journal. **6** (3), 78–84 (1996).

[25] Frederickson P., Kaplan J. L., Yorke E. D., Yorke J. A. The Liapunov Dimension of Strange Attractors. Journal of differential equations. **49**, 185–207 (1983).

Комп'ютерне моделювання впливу мемристивного електромагнітного випромінювання на п'ятивимірну нейронну мережу

Копп М. Й.

Інститут монокристалів, Національна академія наук України, пр. Науки 60, 61072 Харків, Україна

У цьому дослідженні представлено нову архітектуру мемристивної нейронної мережі, що складається з п'яти нейронів, з'єднаних з одним неідеальним мемристором, керованим магнітним потоком. Мемристор моделює вплив зовнішнього електромагнітного випромінювання на перший нейрон. Було проведено комплексний динамічний аналіз, що включав побудову біфуркаційних діаграм як функцій керуючого параметра мемристора та параметра втрат магнітного потоку. Обчислено показники Ляпунова та розмірність Каплана–Йорке для характеристики виявленого хаотичного атрактора. Чисельне моделювання дозволило візуалізацію через фазові портрети та діаграми часової еволюції. Хаотичний атрактор демонструє значно від'ємний шостий показник Ляпунова, що вказує на сильне стиснення всередині системи та підтверджує її дисипативну природу з безперервним стисненням об'єму фазового простору. Аналогову схемну реалізацію запропонованої шестивимірної мемристивної системи було впроваджено з використанням стандартних електронних компонентів у середовищі Multisim. Отримані фазові портрети показали відмінну узгодженість з чисельним моделюванням у Mathematica, підтверджуючи теоретичну модель. Для дослідження явищ синхронізації в біологічних нейронних мережах ми розробили зв'язану архітектуру з двох підмережевих мемристивних мереж. Ця конфігурація демонструє перехідну синхронізацію, надаючи розуміння часової динаміки механізмів міжрегіональної координації, що лежать в основі функціонування мозку.

Ключові слова: *штучні нейронні мережі (ШНМ); мемристор; хаотична поведінка; схемотехнічна реалізація; синхронізація.*